A Hybrid 3D Printing for Highly-efficient Nanoparticle Micropatterning

Journal:	*Journal of Materials Chemistry C*
Manuscript ID	TC-COM-01-2023-000168.R1
Article Type:	Communication
Date Submitted by the Author:	16-Feb-2023
Complete List of Authors:	Jambhulkar, Sayli ; Arizona State University - Polytechnic Campus, Systems Engineering Ravichandran, Dharneedar; Arizona State University, Systems Engineering Sundaravadivelan, Barath; Arizona State University, Department of Mechanical Engineering Song, Kenan; Arizona State University, Engineering; ASU POLYTECHNIC

COMMUNICATION

A Hybrid 3D Printing for Highly-efficient Nanoparticle Micropatterning

Sayli Jambhulkar[a], Dherneedar Ravichandran[a], Barath Sundaravadivelan[b], Kenan Song[c*]

Fused deposition modeling (FDM) 3D printing often generates inevitable surface phenomena/defects called the "staircase effect," which involves anisotropic material texture, rough surface topology, and interlayer voids. Besides, the staircase morphology (i.e., interlayer microchannel dimensions and surface roughness) can be well-controlled with essential printing parameters, for example, layer height and print orientation. Here, staircase surface defects generated from FDM 3D printing were utilized as the confined environment to directly assemble 2D nanoparticles (NPs) of MXene as long-range patterned microstructures via a combination with simple direct ink writing (DIW) 3D printing. Based on the layer-by-layer deposition procedure, Mxene NPs were patterned into microfilm with parallelly stacked morphology by combining the confinement effect from surface microchannels, MXene ink quantity control, and NP-substrate interactions. These commonly-regarded surface defects (i.e., staircase effect) from 3D printing demonstrated the potential for large-scale anisotropic patterning of a wide variety of NPs and biomolecules via simple microfluidic forces for structural reinforcement, thermal sensing, microelectronic devices, optical imaging, wireless data transportation, and metasurface applications.

3D printing is also known as additive manufacturing, a technology to manufacture the 3D object through the layer-upon-layer approach, which is unattainable via conventional (subtractive) manufacturing. The 3D printing process contains three significant steps: firstly, the designing of a 3D printing model by computer-aided design (CAD) software; secondly, the slicing of the 3D printing model with desired printing parameters; thirdly, the layer-upon-layer deposition of printing materials; and lastly, possible heat-treatment (e.g., annealing). The American Society for Testing and Materials (ASTM)

International classifies 3D printing technique into six main categories depending on the printing mechanisms, including extrusion-based (i.e., fused deposition modeling (FDM), direct ink writing (DIW)); vat polymerization-based (i.e., stereolithography (SLA), continuous liquid interface production (CLIP), digital light polymerization (DLP)); material jetting-based (i.e., PolyJet, MultiJet, electrohydrodynamic (EHD), aerosol jet); powder bed fusion (PBF)-based (i.e., selective laser melting (SLM), selective laser sintering (SLS)); directed energy deposition (DED)-based (i.e., electron beam melting (EBM), laser engineering net shape (LENS)), and sheet lamination-based (i.e., laminated object manufacturing (LOM)).[1–4] Different materials have been studied in 3D printing, such as polymers, metals, and ceramics, in the form of powders, colloids, solutions, gels, and filaments.[5,6] These materials possess unique mechanical, thermal, electrical, optical, and biomedical properties suitable for broad applications in thermal packaging, microelectronics, and biomedical areas.[7–9]

Even though 3D printing offers different advantages, such as rapid prototyping, fewer material compositions, faster production, product customization, and comprehensive materials selection, each 3D printing technique has certain limitations. For example, the extrusion-based approach generates defects, such as delamination and void formation;[10] vat polymerization technique has limited build size from resins and light control;[11] material jetting-based requires suitable inks, such as viscoelastic properties and wettability with substrates;[12] PBF-based printing generates components that have low mechanical strength and limited surface finish;[13] DED-based printing requires post-processing of components due to high surface roughness;[14] and LOM need decubing with a labor-intensive process.[15] Some defects may significantly deteriorate the performance of the 3D-printed components. However, some of the surface defects can effectively tune surface properties for different applications. For example, FDM 3D printing displays the most widely observed surface phenomena/defects, such as the "staircase effect," which is more noticeable for oblique and curved surfaces.[16,17] Though premature, these surface defects displayed potential as scaffolds/templates for regulating the deposition of anisotropic nanoparticles and biomolecules from their solutions.[18]

[a] Systems Engineering, The School of Manufacturing Systems and Networks (MSN), Ira A. Fulton Schools of Engineering, Arizona State University (ASU), Mesa, AZ, USA 85212

[b] Mechanical Engineering, The School for Engineering of Matter, Transport and Energy (SEMTE), Ira A. Fulton Schools of Engineering, Arizona State University (ASU), Tempe, AZ, USA 85287

[c] The School of Manufacturing Systems and Networks (MSN), Ira A. Fulton Schools of Engineering, Arizona State University (ASU), Mesa, AZ, USA 85212

*Corresponding author, Email: kenan.song@asu.edu

Electronic Supplementary Information (ESI) available: [details of any supplementary information available should be included here]. See DOI: 10.1039/x0xx00000x

For the small-area deposition of NPs on patterned templates (e.g., grooves, microchannel, trenches, pillars), fluid-mediated deposition techniques, including dip coating, spin coating, droplet casting, and microfluidic, have been studied.[19,20] Among them, the microfluidic exhibits many advantages over conventional solution-based deposition approaches, e.g., fast deposition, precise manipulation fluid, low material consumption, and good scalability.[21,22] Also, the topological micropatterns displayed unique functional properties on the surface, which can be enhanced with nanoscale engineering.[23] However, the challenge is that most template manufacturing has been achieved through traditional processing, such as lithography, micromachining, injection molding, and stamping, which can be compatible with programmable NPs deposition into predetermined sites via microforces.[24–27] These techniques are energy intensive, time-consuming, costly, and laborious. On the contrary, 3D printing technology has the potential for high throughput and large-scale nano/micro-manufacturing.[28,29] On top of that, the printed templates can be customized and designed into complex 3D architectures with multifunctionality highly required for many applications.[30]

In our previous research, we demonstrated novel nanomanufacturing via combining 3D printing (i.e., SLA, μCLIP, multiphase direct ink writing (MDIW)) and fluid-mediated deposition for microscale surface patterning and nanoscale particle alignment.[31,32] The 3D-printed templates with microscale gratings acting as anchoring sites allowed the deposition of NPs at predetermined locations from the particle dispersions.[33–35] On the other hand, fluid-mediated deposition utilized interparticle interaction and microfluid forces, such as capillary, van der Waals, and hydrogen bonding without any external field, to assemble nanoparticles onto patterned surfaces.[36,37] In one case, the SLA-printed template anisotropically aligned 1D carbon nanofibers in a layer-by-layer (LbL) manner facilitated by dip coating.[32] To improve the patterning resolution and particle assembly autonomy, μCLIP 3D printing was used in another case study to generate the template with less surface roughness and combined with capillary-induced deposition for well-stacked patterning of 2D MXene flakes.[31] Additionally, in the MDIW, the selective etching of the sacrificial layer generated high aspect-ratio boron nitride micropatterns. Unlike traditional top-down and bottom-up methods, 3D printing and fluid-mediated deposition enabled complex micropatterning and alignment of 1D and 2D NPs in a simple, rapid, scalable, and cost-effective manner.[31,32] Employing patterning and aligning of NPs into 3D architectures, the performance and application range of topological micropatterns can be enhanced. Our previously reported 3D printing processes involved multi-step manufacturing, limited to photosensitive materials, and required post-processing (i.e., curing, washing, and etching). Comparatively, FDM is a faster, single-step process, suitable for a wide range of thermoplastics as substrate materials, and requires minimum optimization of printing parameters.[38] Thus, this 3D printing-enabled nanoparticle assembly mechanism needs to be investigated in the FDM 3D printing technique for cost-efficient surface patterning and scalable nanoparticle assembly.

In this study, we have developed a novel technique for anisotropic patterning and nanoscale stacking of MXene NPs on the 3D printed substrate by integrating the FDM and DIW 3D printing. First, the FDM 3D printing technique generated the template with microscopic surface topology (reservoirs and microchannels) formed via layer-upon-layer filament deposition. Then, MXene ink was dropped into the reservoir by DIW to understand how template surfaces drive the assembly of NPs inside microchannels. The NPs assembly was induced by capillary and microfluidic forces acting on NPs on the top of the patterned surface to produce microarrays of MXene. By engineering surface defects (i.e., staircase effect), the template surface microstructure, and the resolution of microchannels,
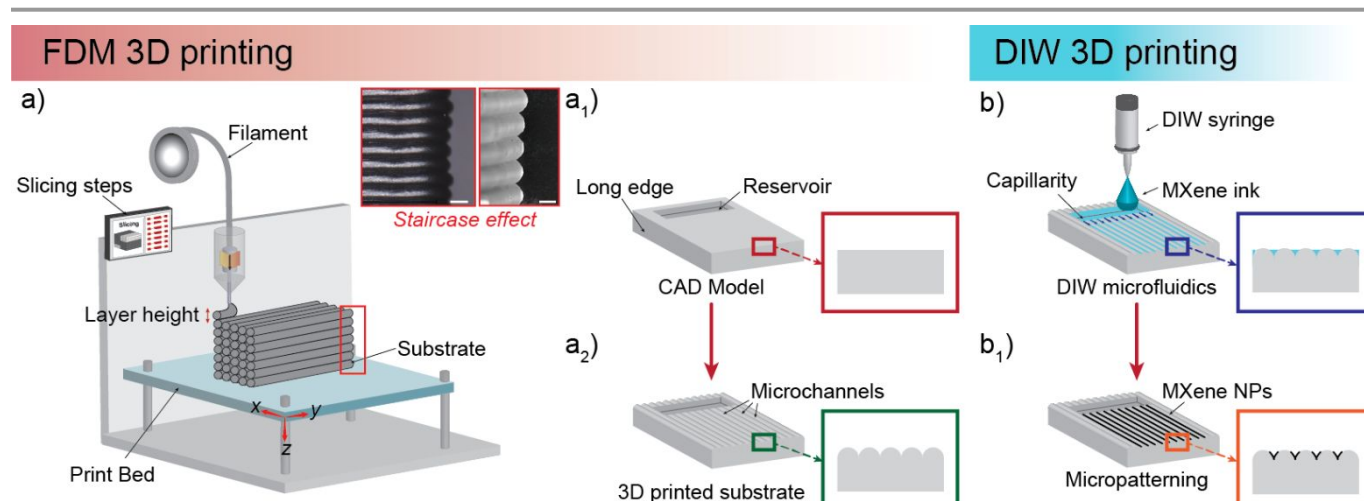

Fig. 1 a-b) The schematic shows the working principle of hybrid processing combining FDM and DIW 3D printing for directed assembly of NPs. a) 3D printing of templates through FDM-heated and -extruded thermoplastic filaments of ABS with staircase effect shown in optical (scale bar 300 μm) and SEM (scale bar 100 μm) images and (b) showing the template effects from DIW-deposited MXene inks. Specifically, a_1) a designed CAD model of a substrate consisting of a reservoir for ink deposition, a_2) the FDM-fabricated template with stair-stepping effects leading to the formation of microchannels on top of the templated surface (e.g., cross-section shapes of the substrate tuned by different FDM printing parameters), b) deposited MXene inks were driven primarily by the capillarity forces within microchannels, and b_1) effects of template topology on MXene nanoparticle assembly efficiency (e.g., particle layer morphologies and layer thicknesses programmable via DIW parameters).

MXene assembly efficiency (e.g., deposition distance, layer thickness, film topology) could be tuned depending on the microchannel characteristics (i.e., layer height (LH)). Additionally, well-aligned and high-aspect-ratio (≈250) patterning of MXene NPs over meso- and macroscale printing shows potential for quick, high throughput, large-scale, and low-cost NPs deposition techniques. See all experimental section details and microforce calculations (**Tables S1-S2**) in the supporting information (SI).

 3D printing surface templates for directed nanoparticle assembly: The patterned templates for subsequent nanoparticle assembly were 3D printed via FDM. Commercial acrylonitrile butadiene styrene (ABS) filaments that went through the FDM printhead were heated closer to 235° C (recommended extrusion temperature) and extruded through a nozzle onto the printing platform, as shown in **Fig. 1a**. As a result, the surface topology was controlled by depositing extruded filaments on the printing platform in a layer-upon-layer fashion. As known, most FDM methods deposit material as flat layers, which result in a "staircase" effect (**Fig. 1a**) on non-vertical or horizontal surfaces and may mechanically compromise part strength because of adhesion weakness between the laminations. Compared to these generally treated defects of staircases (**Fig. 1a**), this research intentionally created

these features (e.g., cross-section contours, individual layer thickness, texture along printing directions) for directed nanoparticle assembly. During FDM printing, the melted ABS filament solidified immediately upon deposition due to the temperature difference between the extrusion nozzle and the substrate in the ambient atmosphere (i.e., RT). Specifically, the computer-aided design (CAD) model consisting of the flat substrate and a reservoir for the MXene ink deposition was first designed, as shown in **Fig. 1a1**. Then, the surface feature was printed along the longer edge of the substrate to control the polymer layer orientation. As represented in **Fig. 1a2**, the 2D design of the substrate was printed into 3D morphology with the "staircase defects" formed in layer-manufactured microchannels. The template surface topology and resolution of microchannels (depth (D) and width (W)) were adjustable depending on the dimensions of the printing layers (i.e., LH). The FDM 3D printing fabricated the template in a layer-upon-layer manner, with the surface template consisting of an ink reservoir connecting to microchannels. The microchannels acted as material feeding sites for MXene NPs to form long-range ordered microstructures via the LbL deposition of MXene inks during DIW printing (**Fig. 1b**). Due to the capillary action and microfluidic forces, the NPs were transported, confined, and oriented within the microchannels to produce MXene
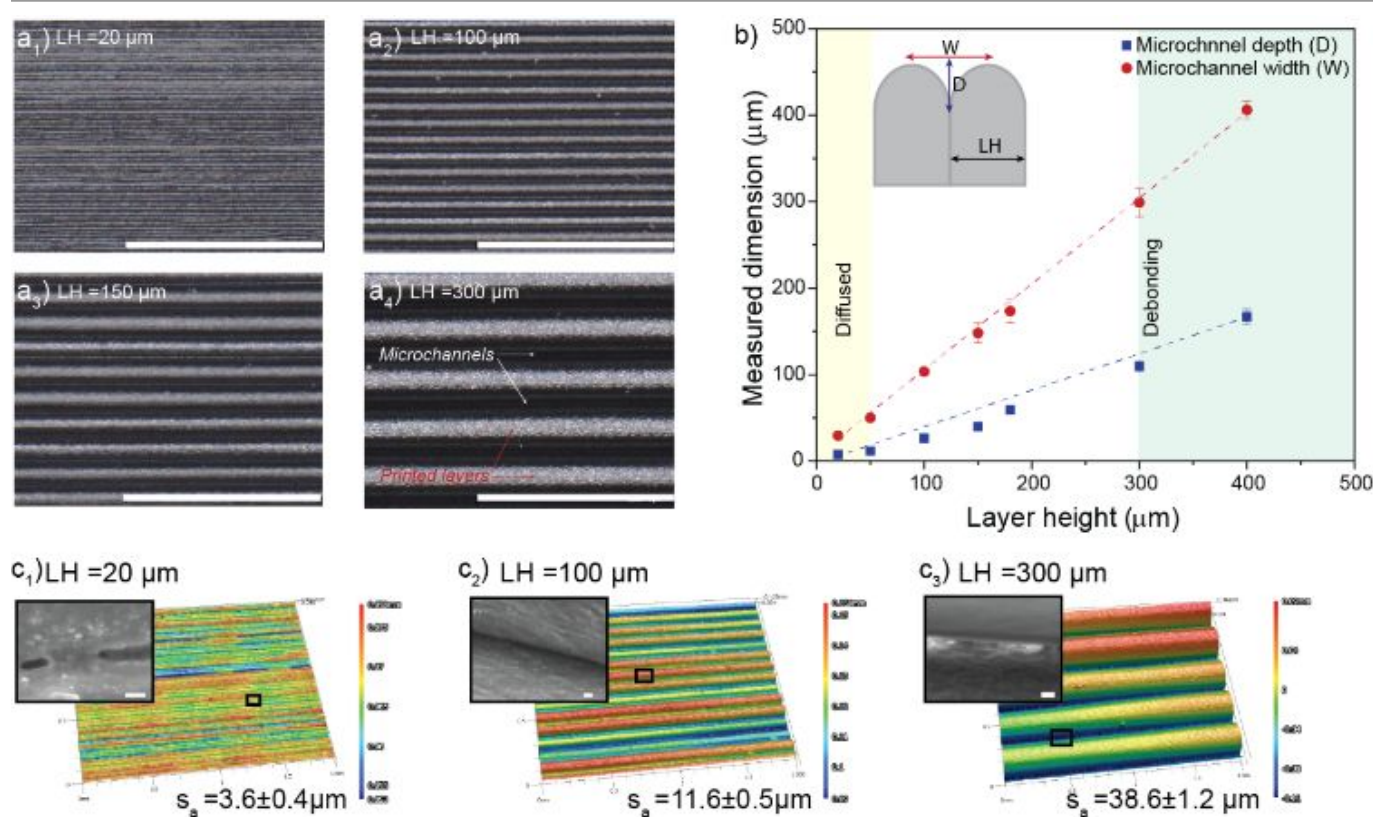

Fig. 2 Surface template morphologies. a1-a4) Optical images of FDM 3D-printed substrates having different layer LH values (i.e., 20, 100, 150, and 300 μm) with the white region as the FDM-printed layer and the black region as microchannels (scale bar 1200 μm), b) measured dimensions of microchannels (i.e., D and W) depending on the LH control, showing the layer diffusion and inconsistency below 50 μm and layer debonding above 300 μm and defining our printing window to be [50 μm, 300 μm]. Furthermore, the surface profile characterizations validated this surface template printability in the confocal optical microscope (COM) and SEM imaging in c1-c3), with the COM showing the printing roughness (i.e., an average roughness values of ≈3.6 μm, 11.6 μm, and 38.6 μm as a result of the staircase effect for LH ≈20, 100, and 300 μm) and zoomed-in SEM images showing the different interfacial behaviors, namely, the diffused, clear, and debonded interfaces (scale bars of 2 μm in SEM images).

nanoparticle microarrays (**Fig. 1b$_1$**). The evolution of surface topology and composition at different processing stages, such as during the reservoir creation, surface patterning, DIW ink deposition, MXene micropatterning, and their influences on nanoparticle assembly, will be discussed in the subsequent sections.

Due to the FDM printing limitations, the template surface morphology and resolution were determined by the layer height. Therefore, samples with different LH values, such as 20, 50, 100, 150, 180, 300, and 400 µm, were printed (**Fig. S1-S2**). The "staircase effect" generated by the additive manufacturing process led to contour-like patterns of the printed substrates, as shown in **Fig. 2a**, where the interlayer spacing increased with the LH. As confirmed by optical profilometer measurements, LH values were close to the theoretical predictions, which proved the accuracy and consistency of the 3D printing system (**Fig. S1**). The contour-like staircase features were anisotropic, desirable for directed NPs assembly useful for heterogeneous mass transport (e.g., limited electron or phonon scattering). The cross-sectional scanning electron microscope (SEM) images provided additional information about the staircase morphology as well as the dimension of the microchannels (**Fig. S2**). The staircase effect generated the microchannels (black region) between adjacent printed layers (white area), which showed sine-wave shape morphology with the variation in microchannels D and W. The D and W linearly increased as a function of the LH with a rough slope of one, as represented in

Fig. 2b. For LH= 20 and 300 µm, the average depth was measured as D ≈7.5 and ≈110 µm, respectively. The width of microchannels was measured as W ≈30, 103, 148, and 300 µm for LH= 20, 100, 150, and 300 µm, respectively. Lower LH (i.e., < 50 µm) resulted in structures with smooth surface finish (surface roughness (S_a) ≈3.6 µm) due to more closely packed layers, as shown in 3D imaging (**Fig. 2c$_1$**). Similarly, higher LH displayed increased S_a generated on the printed substrate surface (**Fig. S3**). For example, staircase surface morphology was observed in LH= 100 and 300 µm samples with an average S_a of ≈11.6 and 38.6 µm, as shown in 3D images (**Fig. 2c$_2$-c$_3$**). The structural defects between the adjacent layers for different LH were identified through SEM analysis (inset imaging in **Fig. 2c**). For LH<50 µm, there were interlayer diffusions due to molten molecular chain movement among densely packed layers (**Fig. 2c$_1$**). On the other side, for LH>300 µm, poor bonding between the adjacent layers was caused possibly by uneven heating which led to the formation of micro gaps or voids at the interface (**Fig. 2c$_3$**). The layer delamination along the printing plane normal has been the most prominent defect in FDM 3D printing, which influences the transverse mechanical properties of the components (i.e., fracture toughness and strength).[39,40] As compared, although smaller LH minimized the voids in the FDM 3D printed substrates, it also negatively affected the production efficiency.[41] As LH decreased, the number of layers required to print the same-dimension substrates increased (i.e., 500, 100, and 33 layer numbers for LH 20, 100, and 300 µm,
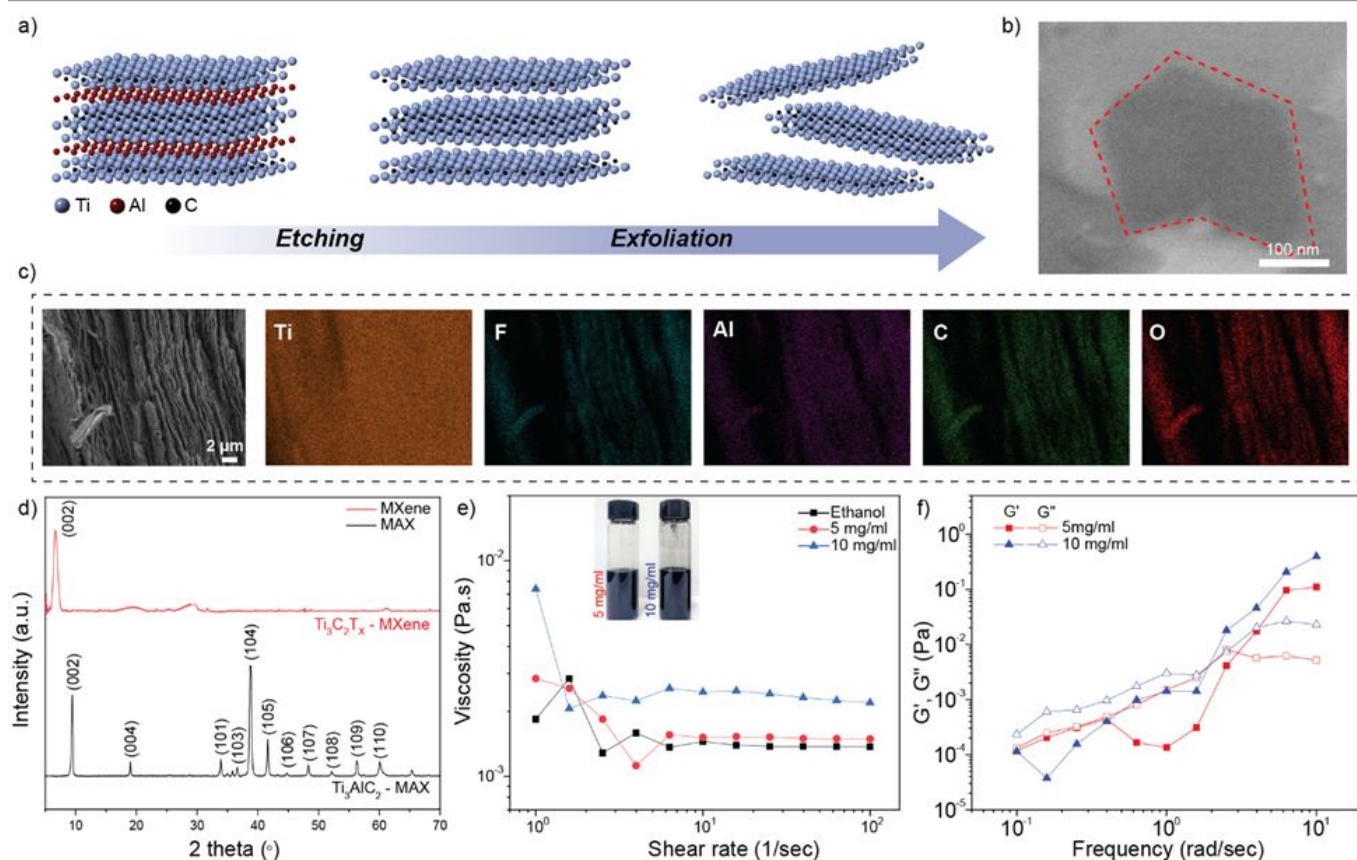
Fig. 3 a) The schematic showing the chemical etching and exfoliation process of Ti$_3$AlC$_2$ during the syntheses of MAX powders and MXene nanoparticles, b) SEM image showing the MXene surface flatness, and c) SEM image and EDS scanning of MXene cross-section showing the layered morphology of nanoflakes, d) XRD spectra of MAX phase and MXene nanoflakes, e) viscosity of MXene/ethanol inks as a function of shear rates (1-100 1/sec), and f) viscoelastic properties (G' and G") of MXene/ethanol inks as a function of frequency (rad/sec).

respectively), leading to lower manufacturing rates. Therefore, this research focuses on the optimized printing parameter (i.e., LH= 100 μm used as one example) to demonstrate directed nanoparticle assembly due to well-controlled surface topology, distinct interfaces, consistent microchannels, and predictable microforces.

MXene synthesis with tunable particle dimensions and physics: The 2D MXene flakes were synthesized by the selective chemical exfoliation of the Al layer from the Ti_3AlC_2 MAX phase, as described in the experimental section. The crystal structure changes during the chemical etching and exfoliation process are represented in **Fig. 3a.** First, the Ti_3AlC_2 MAX phase powder was prepared by mechanical milling followed by heat treatment, which displayed closed stacked and layered morphology (**Fig. S4a**). Next, the MAX phase was etched using a mixture of lithium fluoride (LiF) salt and hydrochloric acid (HCl) for etching the Al layer and obtaining the multilayered accordion-like MXene (**Fig. S4b**). Then, the etched multilayers were exfoliated into single- and few-layered MXene flakes by sonication and centrifugation, as shown in **Fig. 3b,** with an average lateral size of ≈500 nm and thickness of ≈7.5 nm (**Fig. S5**). The MXene nanoflakes film after filtration showed stacking morphology with small interlayer spacing. The energy dispersive spectroscopy (EDS) mapping confirmed the successful removal of Al and the formation of oxygen and fluorine surface termination with the homogenous distribution of Ti, C, O, and F (**Fig. 3c**). The well-exfoliated MXene structures were also reflected in the X-ray diffraction (XRD) spectra of the precursor MAX phase and MXene nanoflakes. For example, the delamination of $Ti_3C_2T_x$ MXene displayed the distinct peak shift for (002) characteristic peak from 9.43° (MAX) to 6.73° (MXene) due to increased interlayer spacing with the disappearance of crystalline peaks near 40.0° (**Fig. 3d**). Additionally, the broadening of the (002) peak suggested an increase in d-spacing (9.37 to 13.26 Å, calculated by **Eqn. S1**) and a decrease in the thickness of $Ti_3C_2T_x$ layers.

The MXene flakes owing to their hydrophilic nature, show excellent dispersibility in water, ethanol, and many other solvents.[42] Here, the $Ti_3C_2T_x$ MXene nanoflakes were added in ethanol because it has low surface tension, good wettability, and a fast evaporation rate. The MXene/ethanol dispersion was prepared by sonicating for 15 min, resulting in a mixture (i.e., 5 and 10 mg/ml) with excellent stability without any macroscopic precipitates or aggregation even 24 hr after preparation (**Fig. 3e**). In addition to dispersion homogeneity, the rheological properties of the inks were significant properties ensuring the successful deposition and patterning of NPs. The viscosities of the ink as a function of shear rate were measured as depicted in **Fig. 3e**. The 5 and 10 mg/ml inks exhibited typical shear thinning behavior, enabling smooth extrusion of MXene ink through the small-diameter DIW nozzle under shear forces and droplet deposition (**Fig. S6**). However, higher MXene particle loading (> 10 mg/ml) would decrease the fluidity of the dispersion due to the increased aggregation of NPs via hydrogen and van der Waals bonding.[43] The viscoelastic properties of the inks were also investigated by performing an oscillation sweep at a constant strain rate. The storage modulus (G') and loss

modulus (G") of the inks were recorded as a function of frequency (rad/sec) at fixed stress 0.015 Pa (**Fig. 3f**). The inks showed the transition from a liquid to solid-like nature at frequencies of ≈3 and 1.9 rad/sec for 5 and 10 mg/ml, respectively. The frequency increase in gelation could probe microstructural rearrangement with the solidification of ink at shorter time scales.[44] The magnitude of modulus increased with the ink concentration, indicating higher interparticle interaction, which would cause crowding of NPs.[45] The dominance of G" over G' displayed that the MXene/ethanol dispersion was suitable for high shear-rate processing methods via solution-based deposition approaches. These rheological characteristics were thus ideal for processing low-concentration inks without causing clogging of printhead and patterned features.

Directed 2D MXene Assembly: The primary principle for the directed nanoparticle assembly involves the (i) confinement of nanoparticles to reduce interparticle interactions (e.g., van der Waals, electrostatic, hydrogen bonding), (ii) capillarity-driven mass transport to distribute along microchannels (**Eqn. S2**), and (iii) shear-stress for 2D plane orientation and stacking (**Eqn. S4 & Table S1**). The width and depth are typical structural features of microchannels tunable during 3D printing (**Fig. 2**). For example, **Fig. 4a-b** explains the effect of microchannel dimensions on the transport of MXene inks. Regardless of the MXene/ethanol concentrations in inks, the substrate with a deeper/higher aspect ratio (i.e., D/W) microchannels transported MXene ink to a longer distance from the 500 μm-deep reservoirs into the microchannels due to larger capillary force (**Fig. 4a-b**). The microfluidic deposition of ink satisfied the Concus-Finn condition for each LH, which describes the spontaneous flow of ink along the microchannel's orientation when the microchannel angle ($\alpha = tan^{-1}(2D/W)$) > the intrinsic contact angle of ink on the flat surface (θ=15.5°) (**Table S2**).[46] During FDM, the depth/aspect ratio of the microchannel was adjusted by the variation of LH from 20-300 μm. A single droplet of 5 μL of MXene ink was dropped into the reservoir, and the transport distance of the nanoparticles was measured. For LH= 100 μm samples, the transport distance was ≈52.29% and 85.18% higher than LH= 50 μm for 5 and 10 mg/ml, respectively. For LH <50 μm, MXene ink could not flow into the microchannel due to the smaller channel depth and frequent interparticle interactions. Besides, layer diffusion could also disrupt the consistency of directed nanoparticle assembly. As LH increased with deeper microchannels, the deposition distances also increased for LH= 50-180 μm because of increased capillary forces and other comparatively negligible microforces (e.g., particle gravity, van der Waals, in **Table S1**). For LH>300 μm, the MXene ink would not be effectively deposited between the channels due to leakage of the fluids from the micro gaps. More importantly, the lack of strict confinement over MXene nanolayers lacked the control of extra momentum (e.g., local fluid turbulence due to printing layer roughness). The effect of NPs loading on the transport distance of MXene ink was also investigated, which showed that for less viscous ink, the transport distances were more prolonged across the microchannel (**Fig. 4c**). For example, the transport

distance for 10 mg/ml was shorter than in LH= 100 µm due to more vital interparticle interactions. The transport velocity of MXene ink transport for LH =100 µm was calculated as ≈0.3 and ≈0.1 mm/sec for 5 and 10 mg/ml, respectively.

The ANSYS Fluent simulation was performed to verify the influence of microchannel dimensions on MXene ink distribution. The analysis determined the volume distribution of 5 mg/ml MXene ink into microchannels of different dimensions (i.e., LH 50, 100, 150, 180 µm, and 20 mm length) via capillary action. **Fig. 4d** demonstrates that the higher capillary force for high LH microchannels (**Table S2**) favoured the spreading of MXene ink into microchannels and thus higher volume of ink was driven into the microchannel. The increase in the aspect ratio of microchannels resulted in the rapid spreading of MXene ink from LH 50 to 180 µm, similar to experimental observations. These simulation results proved the effectiveness of capillary

action in driving MXene ink into 3D-printed templates in an autonomous fashion.

For 3D printed microelectronics, the straight-line micropatterns of different widths, gaps, and thicknesses are essential for high-performance devices. By carefully designing the FDM templates and programming ink rheology, linear or circular micropatterns of conductive NPs can be directly assembled, leading to value-added functions (e.g., electrical conductivity or heat transfer). The optical image shows the MXene NPs were trapped within the microchannel via capillary action for a single droplet of MXene ink of 5 µL. Multiple droplets (DIW printing cycles, #n) of MXene inks were deposited into the reservoir to obtain the uniform deposition of MXene NPs (**Fig. S7**). The optical images show the distinct change in the deposition morphology from a non-uniform deposition for #1 to a continuous deposit for #10 (**Fig. 4e$_1$-e$_2$**) after the evaporation
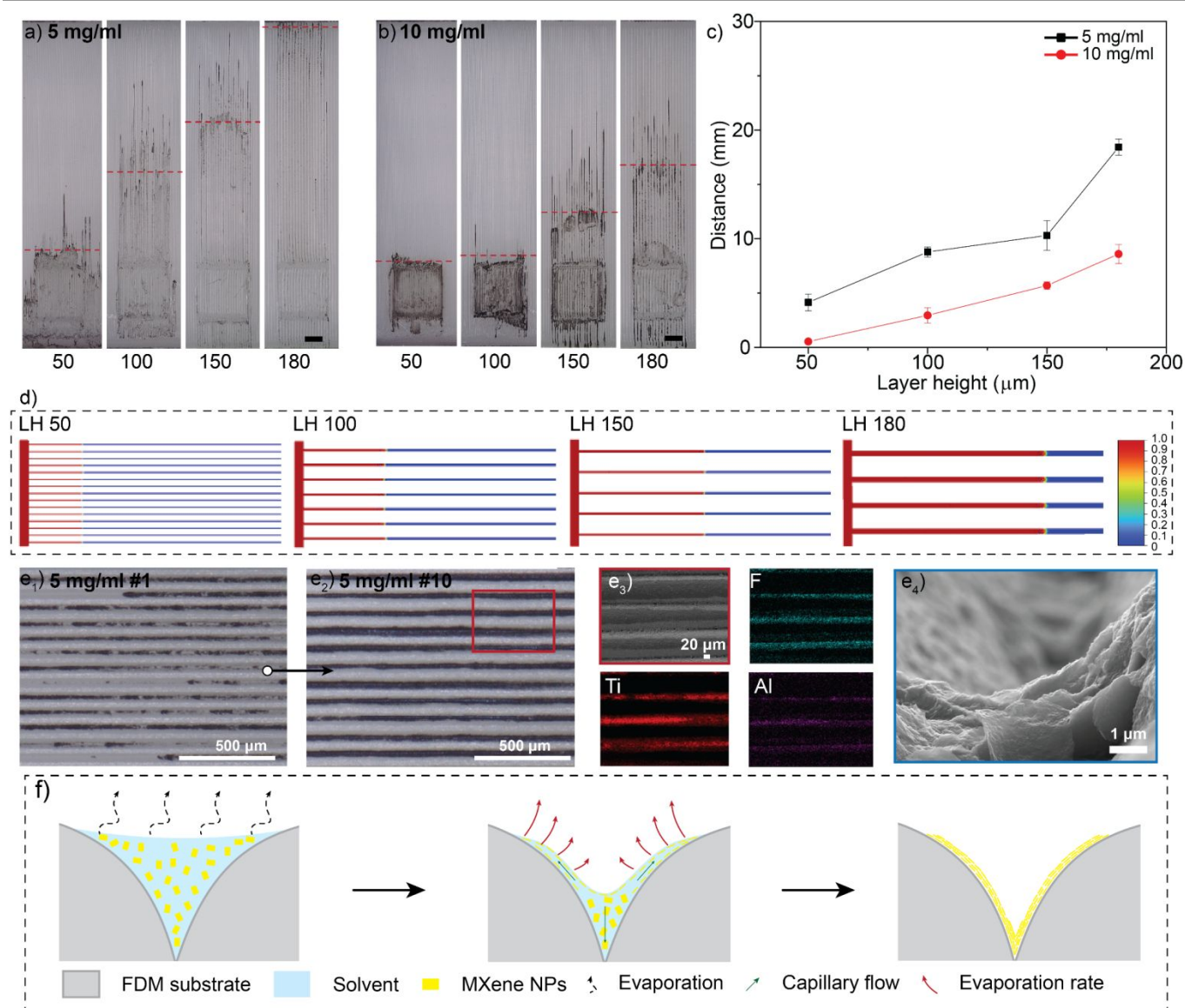
Fig. 4 Optical imaging of the MXene ink transport distances along microchannels from the DIW-deposited 5 µL size droplets for a) 5 mg/ml and b) 10 mg/ml MXene/ethanol colloids with varying surface LH (i.e., 50, 100, 150, and 180 µm) (scale bar 1200 µm), c) distance travelled from the MXene inks driven via the capillary action showed consistent increase as a function of LH but decreased as a nanoparticle concentration, d) ANSYS Fluent simulation reults of MXene ink (5 mg/ml) transported within microchannels of different LH via the capillary effect (scale bar represents the volume fraction of MXene ink) , e$_1$-e$_4$) optical, SEM and EDS maps showing the surface topography and parallel stacking of MXene NPs deposited into microchannels with 100 µm LH for 5 mg/ml MXene inks, and f) schematics describing the mechanism of MXene NPs deposition and assembly.

of ethanol at RT. The successive sediment of MXene ink droplets, followed by the evaporation of ethanol, and a thin layer of MXene NPs deposited into cm-scale microchannels proved the nano-manufacturability and assembly efficiency of long-range anisotropic microstructures. For example, the linear micropatterns of MXene NPs of width ≈41 µm, gaps ≈54 µm, and an aspect ratio of ≈250 can be quickly generated within minutes via hybrid manufacturing combining FDM and DIW 3D printing techniques. The SEM and EDS mapping also confirmed the formation of linear micropatterns with MXene confinement, smooth surfaces, and particle edge-to-edge connectivity within the microchannels (**Fig. 4e$_3$**). The cross-sectional SEM image of patterned structures also shows the well-stacked and in-plane parallelly aligned MXene flakes formed due to shear-assisted MXene exfoliation (**Fig. 4e$_4$**).

Fig. 4f schematic illustrates the directed assembly mechanism via NPs transportation and stacking, a combination of (i) capillarity from microfluidic, (ii) shear forces from Newtonian fluids, and (iii) gravity from evaporative force-assisted sedimentation.[31,47] Specifically, the nanoparticle micropatterning was initiated by the formation of ink meniscus between the walls of microchannels from the colloidal delivery, where the NPs were accumulated and assembled into millimeter-long arrays (**Fig. 4a-b**). The rapid evaporation of ethanol caused the NPs to sediment at the bottom microchannels, followed by NPs self-assembly via short-range intermolecular forces. As the ethanol displayed good wettability on ABS (i.e., 15.5° (**Fig. S8**), the capillary force was the dominant force for MXene ink deposition compared to other micro forces (e.g., drag force and gravitational force, calculations are provided in **Table S1**).[31] The shear fields within the microchannel promoted the alignment of 2D MXene flakes, considering much smaller gravity, buoyancy, and van der Waals. This is because according to **Eqn. S3**, the Reynolds number (Re) was small (i.e., Re <<1), representing a laminar flow of the ink for smooth and uniform deposition of NPs followed by ethanol evaporation (**Table S2**).[47] Last but not least, this 2D flake orientation was retained during solvent evaporation in the vicinity of the deposition sites. The U-shape meniscus of the confined ink got MXene pinned to the microchannel surface because of the excellent wettability of the ink, and the evaporation of ethanol accelerated the convection towards the meniscus, eventually resulting in the compliance of NPs to the microchannel wall surfaces. During the solvent's evaporation, the inks' viscosity increased, and particles were sedimented within the microchannels. The rigid 2D layers caused localized compliance of MXene to the microchannel walls in the form of a thin film. After the first layer deposition, the lateral capillary force would work between the adjacent NPs due to the Laplace pressure gradient to connect MXene edge-to-edge in subsequent assembly (**Fig. S9**).[48] The shearing of NPs followed by short-range forces, such as microcapillary force and van der Wall force, resulted in the long-range in-plane and out-of-plane ordering of NPs with high assembly effectiveness.[49] This technique shows massive potential for the deposition of different nanoparticles and possible biomolecules with directed assembly at the microscale (**Fig. S10**).

The staircase effects, usually treated as manufacturing defects in 3D printing, can be utilized as an effective template for the selective deposition, preferential orientation, and anisotropic placement of MXene NPs. By optimizing the FDM printing parameters (e.g., contour profiles, LH, print orientation), the surface topology (i.e., microchannels) on the top of the template can be created. The programmable 3D microchannels of different dimensions were shown to be effective for directional nanoparticle assembly. The drying of ethanol within microchannels formed a meniscus between the sidewalls of microchannels, driving the NPs toward the bottom of the meniscus within the confined region. This research showed the combination of FDM 3D printing for designing surface topography with DIW 3D printing for templated NPs self-assembly. The resolution of microchannels, the viscosity of MXene inks, and NPs-substrate interactions were critical parameters for the confinement, alignment, and edge-edge interconnections among patterned MXene flakes. With this defect engineering strategy, many nanoparticles and biomolecules having a structurally anisotropic nature can be potentially patterned into long-range orders for broad applications.

References

1 C. M. Thakar, S. S. Parkhe, A. Jain, K. Phasinam, G. Murugesan and R. J. M. Ventayen, *Materials Today: Proceedings*, 2022, **51**, 842–849.
2 W. Xu, S. Jambhulkar, Y. Zhu, D. Ravichandran, M. Kakarla, B. Vernon, D. G. Lott, J. L. Cornella, O. Shefi, G. Miquelard-Garnier, Y. Yang and K. Song, *Composites Part B: Engineering*, 2021, **223**, 109102.
3 M. Manoj Prabhakar, A. K. Saravanan, A. Haiter Lenin, I. Jerin leno, K. Mayandi and P. Sethu Ramalingam, *Materials Today: Proceedings*, 2021, **45**, 6108–6114.
4 S. Park, W. Shou, L. Makatura, W. Matusik and K. (Kelvin) Fu, *Matter*, 2022, **5**, 43–76.
5 R. Ranjan, D. Kumar, M. Kundu and S. Chandra Moi, *Materials Today: Proceedings*, 2022, **61**, 43–49.
6 A. M. E. Arefin, N. R. Khatri, N. Kulkarni and P. F. Egan, *Polymers*, 2021, **13**, 1499.
7 X. Wang, M. Jiang, Z. Zhou, J. Gou and D. Hui, *Composites Part B: Engineering*, 2017, **110**, 442–458.
8 U. Kalsoom, P. N. Nesterenko and B. Paull, *RSC Adv.*, 2016, **6**, 60355–60371.
9 J. Saroia, Y. Wang, Q. Wei, M. Lei, X. Li, Y. Guo and K. Zhang, *Int J Adv Manuf Technol*, 2020, **106**, 1695–1721.
10 Y. Tao, F. Kong, Z. Li, J. Zhang, X. Zhao, Q. Yin, D. Xing and P. Li, *Journal of Materials Research and Technology*, 2021, **15**, 4860–4879.
11 A. Al Rashid, W. Ahmed, M. Y. Khalid and M. Koç, *Additive Manufacturing*, 2021, **47**, 102279.
12 S. Mora, N. M. Pugno and D. Misseroni, *Materials Today*, 2022, **59**, 107–132.
13 M. Ziaee and N. B. Crane, *Additive Manufacturing*, 2019, **28**, 781–801.
14 M. Lalegani Dezaki, A. Serjouei, A. Zolfagharian, M. Fotouhi, M. Moradi, M. K. A. Ariffin and M. Bodaghi, *Advanced Powder Materials*, 2022, **1**, 100054.
15 B. Dermeik and N. Travitzky, *Adv. Eng. Mater.*, 2020, **22**, 2000256.

16 H. Guo, J. Xu, S. Zhang and G. Yi, *Applied Sciences*, 2020, **11**, 304.

17 S. Wickramasinghe, T. Do and P. Tran, *Polymers*, 2020, **12**, 1529.

18 S. Miao, M. Nowicki, H. Cui, S.-J. Lee, X. Zhou, D. K. Mills and L. G. Zhang, *Biofabrication*, 2019, **11**, 035030.

19 D. Baranov, A. Fiore, M. van Huis, C. Giannini, A. Falqui, U. Lafont, H. Zandbergen, M. Zanella, R. Cingolani and L. Manna, *Nano Lett.*, 2010, **10**, 743–749.

20 M. Grzelczak, J. Vermant, E. M. Furst and L. M. Liz-Marzán, *ACS Nano*, 2010, **4**, 3591–3605.

21 A. Olanrewaju, M. Beaugrand, M. Yafia and D. Juncker, *Lab Chip*, 2018, **18**, 2323–2347.

22 N. Bhattacharjee, A. Urrios, S. Kang and A. Folch, *Lab Chip*, 2016, **16**, 1720–1742.

23 H.-N. Barad, H. Kwon, M. Alarcón-Correa and P. Fischer, *ACS Nano*, 2021, **15**, 5861–5875.

24 D. Lebedev, G. Malyshev, I. Ryzhkov, A. Mozharov, K. Shugurov, V. Sharov, M. Panov, I. Tumkin, P. Afonicheva, A. Evstrapov, A. Bukatin and I. Mukhin, *Microfluid Nanofluid*, 2021, **25**, 51.

25 L. Jiang and N. S. Korivi, in *Nanolithography*, Elsevier, 2014, pp. 424–443.

26 D. J. Guckenberger, T. E. de Groot, A. M. D. Wan, D. J. Beebe and E. W. K. Young, *Lab Chip*, 2015, **15**, 2364–2378.

27 K. Sugioka, J. Xu, D. Wu, Y. Hanada, Z. Wang, Y. Cheng and K. Midorikawa, *Lab Chip*, 2014, **14**, 3447–3458.

28 W. Xu, S. Jambhulkar, D. Ravichandran, Y. Zhu, M. Kakarla, Q. Nian, B. Azeredo, X. Chen, K. Jin, B. Vernon, D. G. Lott, J. L. Cornella, O. Shefi, G. Miquelard-Garnier, Y. Yang and K. Song, *Small*, 2021, **17**, 2100817.

29 D. Ravichandran, W. Xu, S. Jambhulkar, Y. Zhu, M. Kakarla, M. Bawareth and K. Song, *ACS Appl. Mater. Interfaces*, 2021, **13**, 52274–52294.

30 Y. Zhang, Y. Wang, Q. Jiang, J. K. El-Demellawi, H. Kim and H. N. Alshareef, *Adv. Mater.*, 2020, **32**, 1908486.

31 S. Jambhulkar, S. Liu, P. Vala, W. Xu, D. Ravichandran, Y. Zhu, K. Bi, Q. Nian, X. Chen and K. Song, *ACS Nano*, 2021, **15**, 12057–12068.

32 S. Jambhulkar, W. Xu, D. Ravichandran, J. Prakash, A. N. Mada Kannan and K. Song, *Nano Lett.*, 2020, **20**, 3199–3206.

33 J. R. Tumbleston, D. Shirvanyants, N. Ermoshkin, R. Janusziewicz, A. R. Johnson, D. Kelly, K. Chen, R. Pinschmidt, J. P. Rolland, A. Ermoshkin, E. T. Samulski and J. M. DeSimone, *Science*, 2015, **347**, 1349–1352.

34 L. Lu, P. Guo and Y. Pan, *Journal of Manufacturing Science and Engineering*, 2017, **139**, 071008.

35 Y. Yang, Z. Chen, X. Song, Z. Zhang, J. Zhang, K. K. Shung, Q. Zhou and Y. Chen, *Adv. Mater.*, 2017, **29**, 1605750.

36 T. Brezesinski, M. Groenewolt, A. Gibaud, N. Pinna, M. Antonietti and B. Smarsly, *Adv. Mater.*, 2006, **18**, 2260–2263.

37 P. Zhu, T. Kong, C. Zhou, L. Lei and L. Wang, *Small Methods*, 2018, **2**, 1800017.

38 D. Rahmatabadi, A. Aminzadeh, M. Aberoumand and M. Moradi, in *Fused Deposition Modeling Based 3D Printing*, eds. H. K. Dave and J. P. Davim, Springer International Publishing, Cham, 2021, pp. 131–150.

39 H. Gonabadi, A. Yadav and S. J. Bull, *Int J Adv Manuf Technol*, 2020, **111**, 695–709.

40 H. Kim, K.-H. Ryu, D. Baek, T. A. Khan, H.-J. Kim, S. Shin, J. Hyun, J. S. Ahn, S.-J. Ahn, H. J. Kim and J. Koo, *ACS Appl. Mater. Interfaces*, 2020, **12**, 23453–23463.

41 J. Wu, *IOP Conf. Ser.: Mater. Sci. Eng.*, 2018, **392**, 062050.

42 K. Maleski, V. N. Mochalin and Y. Gogotsi, *Chem. Mater.*, 2017, **29**, 1632–1640.

43 X. Meng, Y. Sun, M. Yu, Z. Wang and J. Qiu, *Small Science*, 2021, **1**, 2100021.

44 J. Orangi, F. Hamade, V. A. Davis and M. Beidaghi, *ACS Nano*, 2020, **14**, 640–650.

45 S. Abdolhosseinzadeh, J. Heier and C. (John) Zhang, *J. Phys. Energy*, 2020, **2**, 031004.

46 P. Concus and R. Finn, *Proc. Natl. Acad. Sci. U.S.A.*, 1969, **63**, 292–299.

47 H. Zargartalebi, S. H. Hejazi and A. Sanati-Nezhad, *Nat Commun*, 2022, **13**, 3085.

48 K. Kato, F. Dang, K. Mimura, Y. Kinemuchi, H. Imai, S. Wada, M. Osada, H. Haneda and M. Kuwabara, *Advanced Powder Technology*, 2014, **25**, 1401–1414.

49 D. Luo, C. Yan and T. Wang, *Small*, 2015, **11**, 5984–6008.

Author contributions

Conflicts of interest

There are no conflicts to declare.